Semiautomatic segmentation of aortic valve from sequenced ultrasound image using a novel shape-constraint GCV model

Yiting Guo
Multi-disciplinary Research Center, Hebei University, Baoding 071000, China

Bin Dong
Hebei University Affiliated Hospital, Hebei Baoding 071000, China

Bing Wang
College of Mathematics and Computer Science, Hebei University, Baoding 071000, China

Hongzhi Xie[a)] and Shuyang Zhang
Department of Cardiovascular, Peking Union Medical College Hospital, Beijing 100005, China

Lixu Gu[a)]
Multi-disciplinary Research Center, Hebei University, Baoding 071000, China and School of Biomedical Engineering, Shanghai Jiao Tong University, Shanghai 200030, China

(Received 19 November 2013; revised 19 March 2014; accepted for publication 27 April 2014; published 3 June 2014)

Purpose: Effective and accurate segmentation of the aortic valve (AV) from sequenced ultrasound (US) images remains a technical challenge because of intrinsic factors of ultrasound images that impact the quality and the continuous changes of shape and position of segmented objects. In this paper, a novel shape-constraint gradient Chan-Vese (GCV) model is proposed for segmenting the AV from time serial echocardiography.

Methods: The GCV model is derived by incorporating the energy of the gradient vector flow into a CV model framework, where the gradient vector energy term is introduced by calculating the deviation angle between the inward normal force of the evolution contour and the gradient vector force. The flow force enlarges the capture range and enhances the blurred boundaries of objects. This is achieved by adding a circle-like contour (constructed using the AV structure region as a constraint shape) as an energy item to the GCV model through the shape comparison function. This shape-constrained energy can enhance the image constraint force by effectively connecting separate gaps of the object edge as well as driving the evolution contour to quickly approach the ideal object. Because of the slight movement of the AV in adjacent frames, the initial constraint shape is defined by users, with the other constraint shapes being derived from the segmentation results of adjacent sequence frames after morphological filtering. The AV is segmented from the US images by minimizing the proposed energy function.

Results: To evaluate the performance of the proposed method, five assessment parameters were used to compare it with manual delineations performed by radiologists (gold standards). Three hundred and fifteen images acquired from nine groups were analyzed in the experiment. The area-metric overlap error rate was 6.89% ± 2.88%, the relative area difference rate 3.94% ± 2.63%, the average symmetric contour distance 1.08 ± 0.43 mm, the root mean square symmetric contour distance 1.37 ± 0.52 mm, and the maximum symmetric contour distance was 3.57 ± 1.72 mm.

Conclusions: Compared with the CV model, as a result of the combination of the gradient vector and neighborhood shape information, this semiautomatic segmentation method significantly improves the accuracy and robustness of AV segmentation, making it feasible for improved segmentation of aortic valves from US images that have fuzzy boundaries. © *2014 American Association of Physicists in Medicine*. [http://dx.doi.org/10.1118/1.4876735]

Key words: image segmentation, aortic valve, GCV model, energy optimization, shape constraint

1. INTRODUCTION

The aortic valve (AV) is a vital passageway inside the heart that prevents the backward flow of blood as it is pumped from the left ventricle to the aorta. As a one-way valve, the AV is open or closed in a regular sequence in a normal heart.[1] A recent investigation showed that valvular heart disease (VHD), including aortic regurgitation and aortic stenosis, is a significant threat to human health.[2,3] Aortic regurgitation is caused by a partially closed AV that induces reflux of blood back into the left ventricle, while aortic stenosis results from an incompletely open AV that restricts blood flow into the aorta. In routine clinical diagnosis, echocardiography is a convenient, affordable, and noninvasive tool for observing the shape and movement of the AV. Effective and accurate segmentation of the AV from echocardiography is the basis and precondition

TABLE I. AV opens and closes in a cardiac cycle.

	Phase	Volume	Pressure	AV	Time(s)
Ventricular systole	Isovolumic contraction	Unchanged	↑↑	Closed	0.06–0.08
	Maximum ejection	↓	↑To max	Open	0.11
	Reduced ejection	↓	↓	Open	0.14
Ventricular diastole	Isovolumic relaxation	Unchanged	↓↓	Closed	0.06–0.08
	Rapid filling	↑	↓To min	Closed	0.11
	Reduced filling	↑	↑	Closed	0.19
	Auricular systole	↑	↑	Closed	0.1

to improve the accuracy of intraoperative location in image guided intervention (IGI) for VHD.[4]

Automated or semiautomated segmentation is important clinically to overcome the shortcomings of manual segmentation methods, which suffer from poor repeatability, are lengthy, with results varying from person to person. There are three major difficulties in segmenting AV from ultrasound (US) images. First, the position and shape of AV are changed in adjacent sequence frames as the AV opens and closes during a cardiac cycle (Table I).[5] Second, speckle affects the ability to distinguish details in the image and is the most difficult problem in segmenting US images.[6] Finally, the anisotropy of US image acquisition, artifacts such as shadow from calcification of the leaflets, and attenuation may reduce the quality of data.[7,8]

1.A. Related work

Many automated or semiautomated approaches have been proposed for cardiac US image segmentation.[9,10] In early studies, threshold-based methods[11–13] were used to segment either the preprocessed US image or the original US images, which were mostly based on the analysis of the histogram of absolute differences. However, the histogram-based segmentation does not achieve very accurate results due to the abnormal distribution of gray levels and a different noise in the US images. Klingler *et al.*[13] developed a semiautomatic technique by using the traditional threshold method and mathematical morphology to segment the endocardium in echocardiograms.

The clustering method[14–18] was also applied to segment the cardiac US images. Ruben *et al.*[15] proposed a fuzzy clustering method for left ventricular images classification, in which two attribute criteria (gray level and global information) were employed to segment ventricles. Shanmugam *et al.*[14] presented a fast SQL K-Means clustering algorithm to segment the 2D echo images in apical, four chamber, long-axis and short-axis views, where Euclidean distance computation is the most time-consuming process. Because of the poor quality of US image, the main challenge is how to select suitable classification conditions. Usually, this is a complex and difficult process, and the classification condition is applicable to a small number of the images that have specific features.

In recent years, the energy-based active contour model[19–36] method that was developed to work with blurred boundaries has shown promising segmentation results. The basic idea of the active contour model method is that the evolution contour deforms to the desired segmentation by minimizing the given energy function. There are two major classes of active contour models: edge-based models and region-based models. The edge-based model[21–23] is more suitable for segmentation of images having clear boundaries, where the gradient information of the image is used to stop the evolution contour. The region-based model[24–26] utilizes the global region information of the image, and is suitable for segmenting images with fuzzy boundaries. The key process of this method is to integrate the proper energy corresponding to the image features into the active contour framework. Belaid *et al.*[27] developed a novel segmentation method of the left ventricle within the active contour framework, which used a new speed function based on local phase and local orientation derived from the monogenic signal to detect boundaries in low contrast regions.

While cardiac US image segmentations is an indispensable tool in the analysis of cardiovascular disease, the issues relating to the segmentation of cardiac valves still have not been well addressed. Most of the reported literature involves the use of energy-based active contour algorithms. Shang *et al.*[28] proposed a segmentation method for the cardiac valve structure in US which incorporated preknowledge of the region and shape into a geodesic active contour to guide the curve into the ideal contour. Martin *et al.*[29] presented a semiautomatic method for segmenting the mitral valve leaflet in transesophageal echocardiography images. However, the leaflets of the AV have an almost complete change of position and shape during the opening and closing of the valve during a cardiac cycle, so it remains a challenge to automatically detect AV contours from sequenced echocardiography images. In the paper, a fast segmentation algorithm is constructed by using two constrained active contours and curve fitting techniques. To segment the AV from poor quality US data, this paper presents our research to find the most suitable constraint energy and to integrate it into active contour framework.

1.B. The motivation for our method

The active contour model has shown promising segmentation results even in the presence of speckle, and custom-made constraint energies can be conveniently integrated into the active contour model framework to accurately segment US images of different tissues and organs. Because the basic active contour model is less suitable for segmenting short-axis AV US images, the gradient Chan-Vese (GCV) model is constructed to segment AV US images by combining the gradient vector energy[30,31] into the Chan-Vese (CV) model. The gradient vector energy acts as an effective image force to enhance the weak boundaries and also is somewhat effective at inhibiting overflow at fuzzy boundaries. To solve the difficulties of partial segmentation and overflow, and to reduce clinician workload, the shape information[32,33] of adjacent frames is incorporated into the GCV model energy functional as an additional constraint. Improved AV segmentation may be achieved by minimizing this modified energy functional.

The purpose of this study is to develop a computer-assisted means of extracting the AV from a US image sequence based on the GCV model coupled with shape-constraint energy. The rest of this paper is organized as follows. Section 2 presents the segmentation method in detail, and Sec. 3 describes the database and experimental results. The paper concludes with a discussion of the limitations of the approach and future work in Sec. 4.

2. METHODS

2.A. GCV model

The GCV model is based on the CV model,[25] which is a flexible and powerful method suitable for segmenting many types of images, including the region segmentation with weak boundaries. The model forces the evolution contour C to approach the boundary of the object by minimizing an energy function, which is defined by

$$\begin{aligned} E^{\mathrm{CV}}(C, c_1, c_2) = {} & v.\mathrm{Area}(C) + \mu.\mathrm{Length}(C) \\ & + \lambda_1 \int_{\Omega\mathrm{in}} |u(x, y) - c_1|^2 dxdy \\ & + \lambda_2 \int_{\Omega\mathrm{out}} |u(x, y) - c_2|^2 dxdy, \end{aligned} \tag{1}$$

where u (x, y) denotes a given image, Ωin the region inside the contour C, and Ωout the region outside the contour C. c_1 and c_2 are two scalar variables, c_1 being the average intensity inside C, and c_2 the average intensity outside C. $v \geq 0$, $\mu \geq 0$, $\lambda_1 > 0$, $\lambda_2 > 0$ are the positive parameters, whose recommended settings are $v = 0$, $\lambda_1 = \lambda_2 = 1$, $\mu = 0.15 \times 255^2$ to facilitate the calculation. Here, larger objects are detected by setting a higher value of μ, and smaller objects are detected using lower values of μ. Area(C) calculates the area of the region inside C, and Length(C) the length of C.

Although the CV model demonstrates good performance for most image segmentation applications, the overflow problem still exists at fuzzy boundaries in AV US images. As shown in Fig. 1(a), the AV is difficult to distinguish from

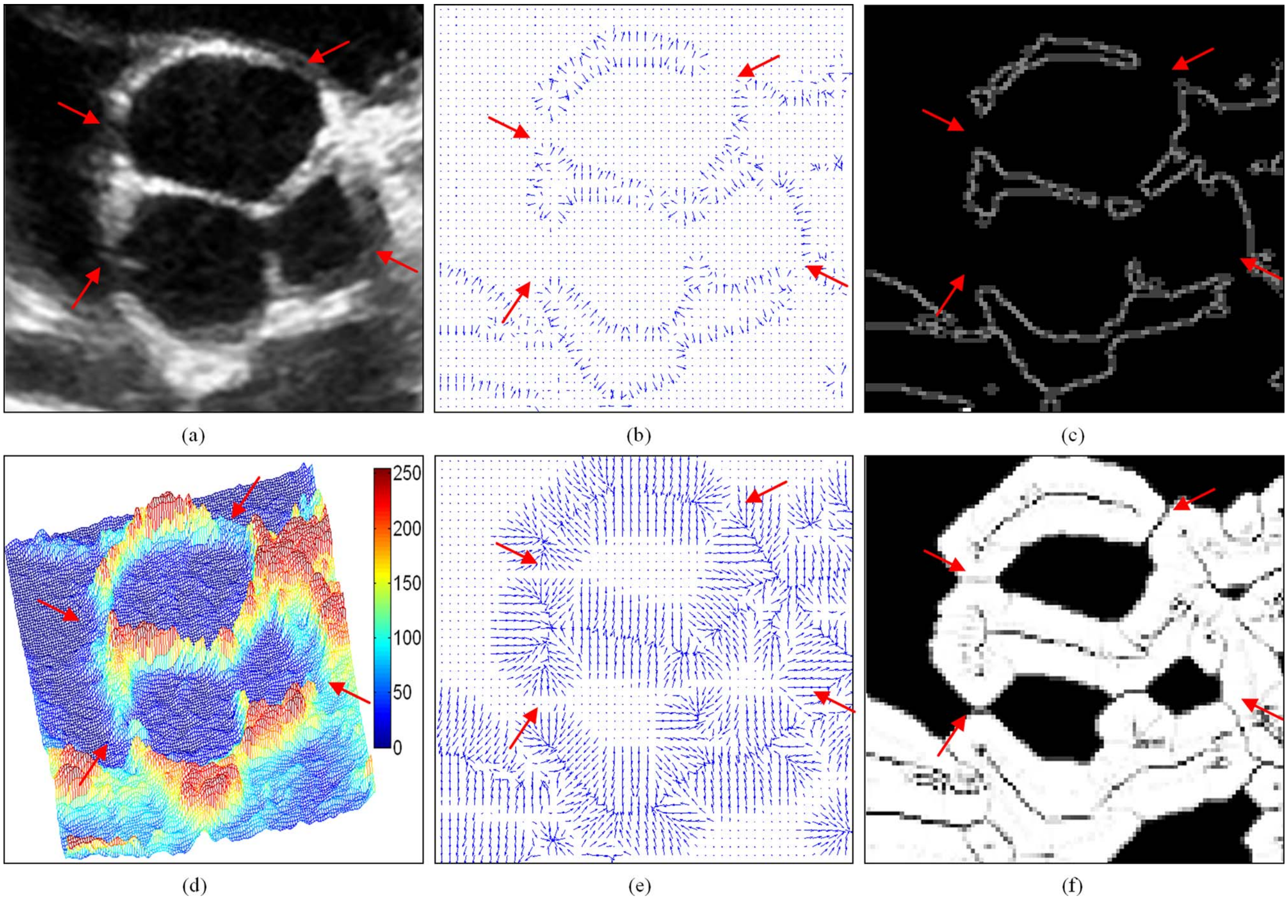

FIG. 1. The difference between traditional potential force field and gradient vector flow field in an AV US image. (a) the original AV US image $I(x, y)$; (b) the traditional potential force field; (c) the edge map of the traditional potential force field: $|\nabla(G_\sigma * I)|^2$; (d) the energy field of the original image; (e) the gradient vector flow field; (f) the edge map of the gradient vector flow field: $|\nabla g|^2$.

other surrounding tissue particularly at the regions indicated by four arrows. If the image is viewed as an energy field [Fig. 1(d)], the image forces drive the evolution contour toward the features where the total energy is minimized. The problem is that the image forces can be almost ignored at the area indicated by four red arrows, where overflow can be a problem at fuzzy boundaries when segmentation is employed using the original CV model.

To overcome the poor convergence problem and limited capture range, an external gradient vector flow force is proposed to enable the active contour to move into the region of interest. The gradient vector flow field[30,31] is defined as $\boldsymbol{g}(x, y) = (u(x, y), v(x, y))$ that minimizes the energy functional

$$E_{gvf}(\boldsymbol{g}) = \iint \eta\left(u_x^2 + u_y^2 + v_x^2 + v_y^2\right) + |\nabla f|^2 |\boldsymbol{g} - \nabla f|^2 dxdy, \tag{2}$$

where η is a regularization parameter and $f(x, y)$ denotes an edge map of the original image $I(x, y)$.

Using the calculus of variations,[37] the Euler equations are expressed as

$$\eta\nabla^2 u - (u - f_x)\left(f_x^2 + f_y^2\right) = 0; \; \eta\nabla^2 v - (v - f_x)\left(f_x^2 + f_y^2\right) = 0, \tag{3}$$

where ∇^2 is the Laplacian operator.

Compared with the traditional potential force field [Figs. 1(b) and 1(c)], the external gradient vector flow force field [Figs. 1(e) and 1(f)] extends the capture range to the entire image domain by diffusing the forces, where the gradient vector flow field inhibits the overflow at blurred boundaries when the AV is segmented from the US image sequence. The addition of the gradient vector flow energy to the CV model is described below.

As shown in Fig. 2, the gradient vector flow field forces the evolution contour to approach the object boundary. When the evolution contour is outside the object boundary (point A of Fig. 2), the concave force acts on the evolution contour; when it is inside this boundary (point B of Fig. 2), the convex force acts on the evolution contour. Under these circumstances, the GCV model can be defined as

$$E^{\mathrm{gcv}}(\phi, c_1, c_2) = \mu \int_{\Omega} \delta(\phi)|\nabla\phi| dxdy + v \int_{\Omega} H(\phi) dxdy + \lambda_1 \int_{\Omega} |u(x, y) - c_1|^2 H(\phi) dxdy + \lambda_2 \times \int_{\Omega} |u(x, y) - c_2|^2 (1 - H(\phi)) dxdy + \alpha \int_{\Omega} - \sin < n(\phi), g > dxdy, \tag{4}$$

where α is a positive parameter that affects curve evolution with gradient vector forces; n is the inward normal vector direction of the evolution contour, g is the direction of the gradient vector.

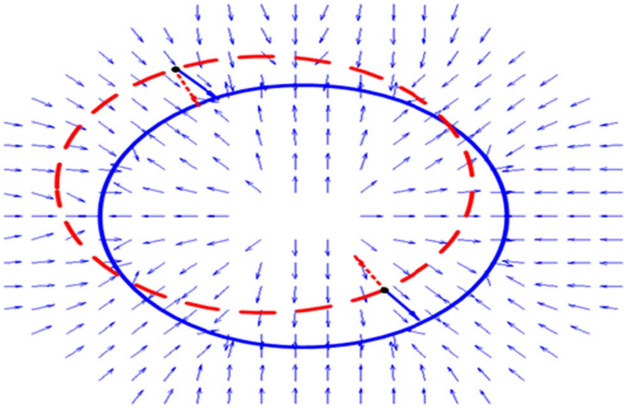

FIG. 2. The dotted ellipse is the active contour, and the solid contour is the feature in the image; the dotted arrows indicate the inward normal vector direction of the evolution contour, and the solid arrows indicate the direction of gradient vector field; Point A and point B are two points on the evolution contour.

2.B. Setting the predefined shapes

Although the gradient vector flow field extends the capture range, it is sensitive to noise. To avoid overflows and partial segmentation, another shape-constraint force acts on the AV image to ensure accurate segmentation. The important issue is how to define the constraint shape.

2.B.1. The initial constraint shape

A cardinal spline interpolation[38] is used to construct the initial constraint shape by four successive control points: P_{m-1}, P_m, P_{m+1}, and P_{m+2}. The endpoints of the segment curve are P_m and P_{m+1}, and the other two points P_{m+1} and P_{m+2} are employed to calculate the slope at endpoints. Four constraint conditions are expressed as

$$\begin{aligned} P(0) &= P_m \\ P(1) &= P_{m+1} \\ P'(0) &= s(P_{m+1} - P_{m-1}) \\ P'(1) &= s(P_{m+2} - P_m). \end{aligned} \tag{5}$$

Using the above four constraint conditions, a cubic polynomial segment curve between these two points can be

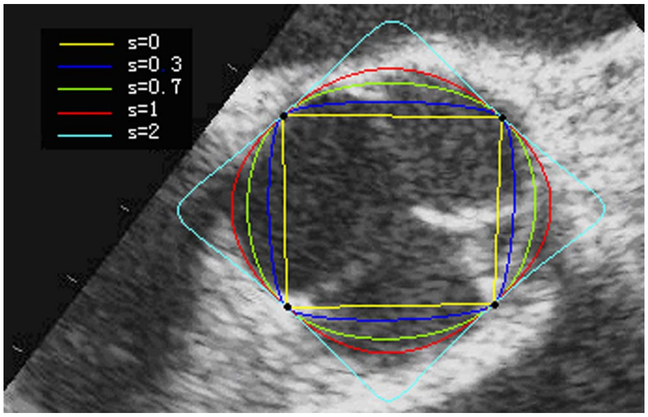

FIG. 3. Four black user-defined points and the closed cardinal spline curves of different colors are constructed by different tension parameter s.

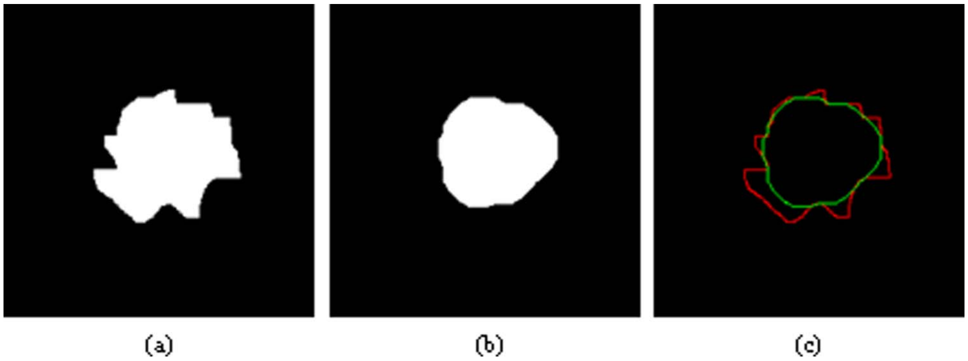

FIG. 4. The rolling ball method: (b) is calculated by the rolling ball operation of (a), where the radius of the spherical structuring element is 20 pixels; the edges of both (a) and (b) is displayed in (c).

expressed as

$$\begin{aligned} P(u) = {} & P_{m-1}(-su^3 + 2su^2 - su) \\ & + P_m[(2-s)u^3 + (s-3)u^2 + 1] \\ & + P_{m+1}[(s-2)u^3 + (3-2s)u^2 + su] \\ & + P_{m+2}(su^3 - su^2), \end{aligned} \tag{6}$$

where s is a tension parameter with effects on the smoothness of the curve.

As shown in Fig. 3, the user defines four black points along the AV borders in the US image, where five closed curves with different colors that pass through four points are produced by cardinal splines interpolation with different tension parameters. To roughly cover the AV, the tension parameter is varied from 0.3 to 1.

2.B.2. Additional constraint shapes

During the cardiac cycle, the AV opens and closes continuously as blood is pumped out of the heart into the aorta. The movement of the AV changes slightly in a relatively fixed region between neighboring images. To improve efficiency and reduce the interaction, constraints apart from the initial shape can be derived from the segmentation results of adjacent frames.

To avoid excessive user interaction, the segmented contour from previous adjacent frame is employed as the constraint shape for current frame. A morphological opening operator,[39] using a disk-shaped structure element (the "rolling ball method") is used to remove details of the contour. Such a smoothed contour can be employed more effectively as a constraint shape.

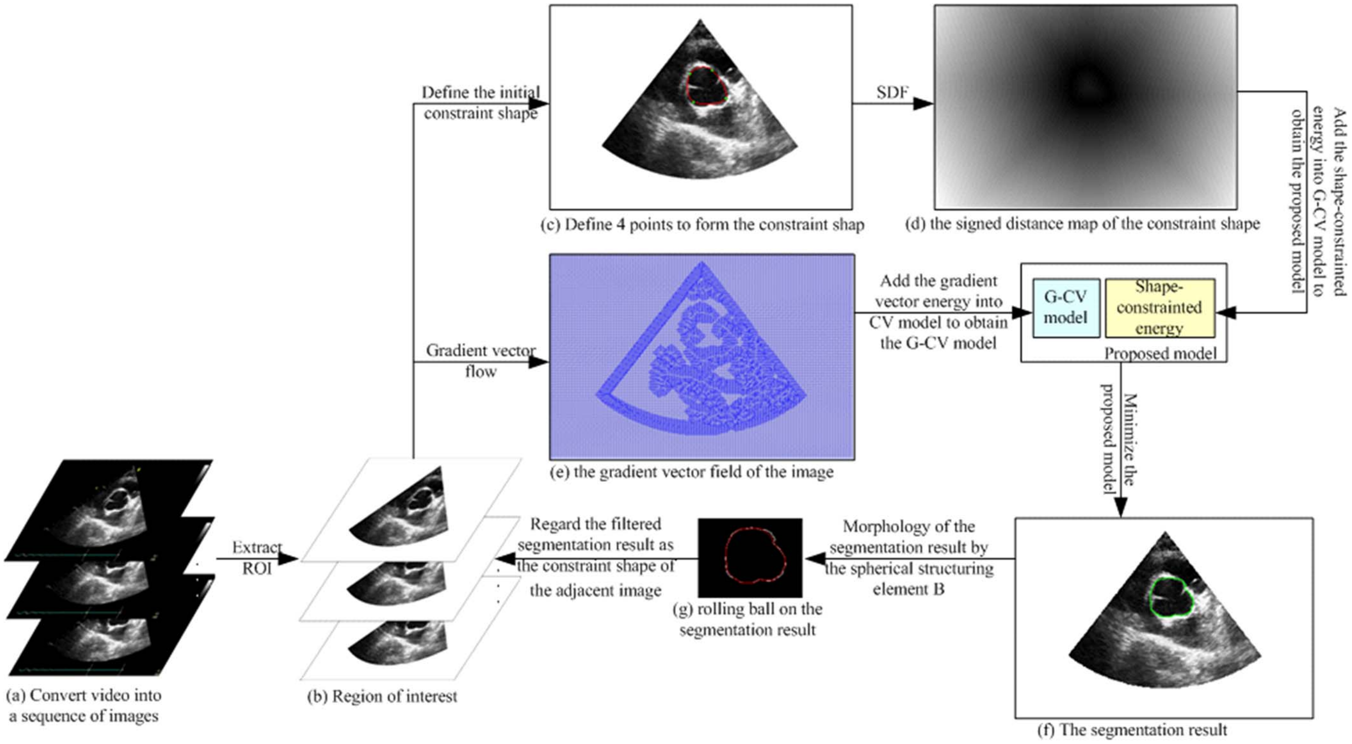

FIG. 5. The workflow of the general experimental framework.

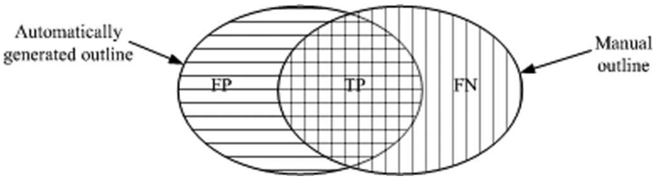

FIG. 6. Regions corresponding to the true positive (TP) region, false positive (FP) region, and the false negative (FN) region.

The application of the rolling ball on the image $F(x, y)$ by the disk-shaped structuring element B is defined as

$$R(F, B) = F \circ B = (F \Theta B) \oplus B. \tag{7}$$

As shown in Fig. 4, the rolling ball method can remove the convex structures and smooth the contours, and is effective in reducing the impact of slightly different shapes and positions on the adjacent AV US sequence. In this way, the constraint shapes are acquired from the segmentation results of adjacent frames by the rolling ball filter.

2.C. The GCV model with shape constraint

Although the GCV model enhances the weak boundaries, overflow at the weak edge of the US image remains. To solve this problem, it is essential to enlarge the image constraint force for connecting separate gaps of the object edge, and the region-based energy constraint is introduced to the GCV model by the shape comparison function: $E_{\text{shape}}(\phi)$. The GCV model with the shape-constraint energy is defined as

$$\begin{aligned} E(\phi, c_1, c_2) &= E^{\text{gcv}}(\phi, c_1, c_2) + \beta E_{\text{shape}}(\phi) \\ &= \mu \int_{\Omega} \delta(\phi)|\nabla\phi| dxdy + v \int_{\Omega} H(\phi) dxdy \\ &\quad + \lambda_1 \int_{\Omega} |u(x, y) - c_1|^2 H(\phi) dxdy \\ &\quad + \lambda_2 \int_{\Omega} |u(x, y) - c_2|^2 (1 - H(\phi)) dxdy \\ &\quad + \alpha \int_{\Omega} - \sin < n(\phi), g > dxdy \\ &\quad + \beta \int_{\Omega} (\phi - \phi_B)^2 dxdy, \end{aligned} \tag{8}$$

where α and β are positive parameters that affect curve evolution with gradient vector forces and shape-driven forces, respectively, and ϕ_B is the signed distance map of the constraint shape. The signed distance map is the product of the signed map and the distance map. In the signed map, the image is divided into two parts by the constraint shape, where the region inside the constraint shape is negative and that outside the constraint shape is positive. The distance map is obtained by calculating the shortest Euclidean distance from each pixel on the image to the constraint shape.

The Euler-Lagrange equation can be implemented by the following gradient descent:

$$\begin{aligned} \frac{\partial\phi}{\partial t} &= \delta(\phi) \left[\mu \text{div} \left(\frac{\nabla\phi}{|\nabla\phi|} \right) - v - \lambda_1 (u - c_1)^2 + \lambda_2 (u - c_2)^2 \right] \\ &\quad + \alpha \frac{\nabla\phi \cdot g}{|\nabla\phi||g|} - 2\beta(\phi - \phi_B) = 0. \end{aligned} \tag{9}$$

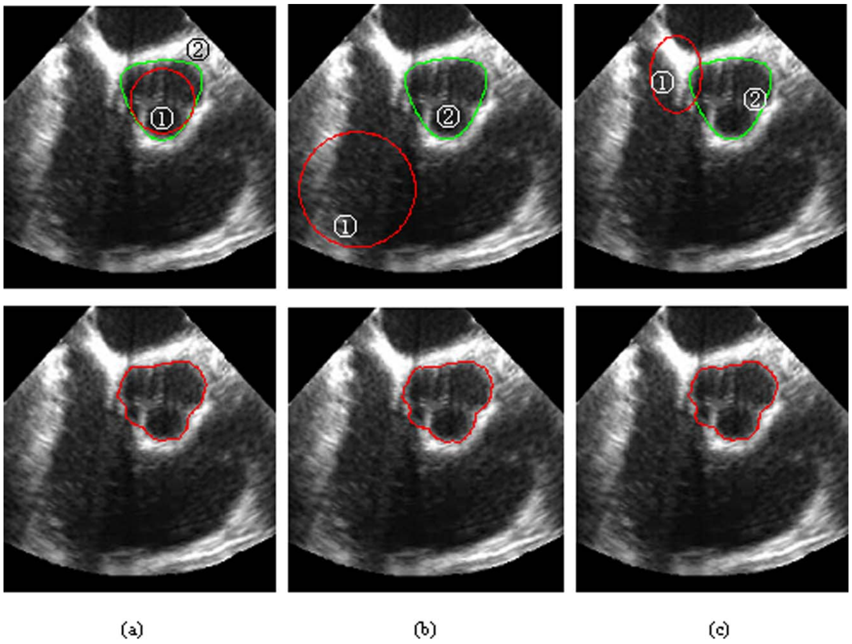

(a) (b) (c)

FIG. 7. An example [image size: 224 × 272 pixels, coordinate (0,0): the upper left corner] shows the influence of the initialization. In the first row, the closed curves ① denote the initial evolution contours (in (a): $(x\text{-}130)^2 + (y\text{-}102)^2 = 22^2$, in (b): $(x\text{-}60)^2 + (y\text{-}170)^2 = 45^2$, in (c): $(3x\text{-}260)^2 + (2y\text{-}160)^2 = 60^{2)}$, and the closed curves ② denote the constraint shapes. In the second row, the curves denote the segmentation results.

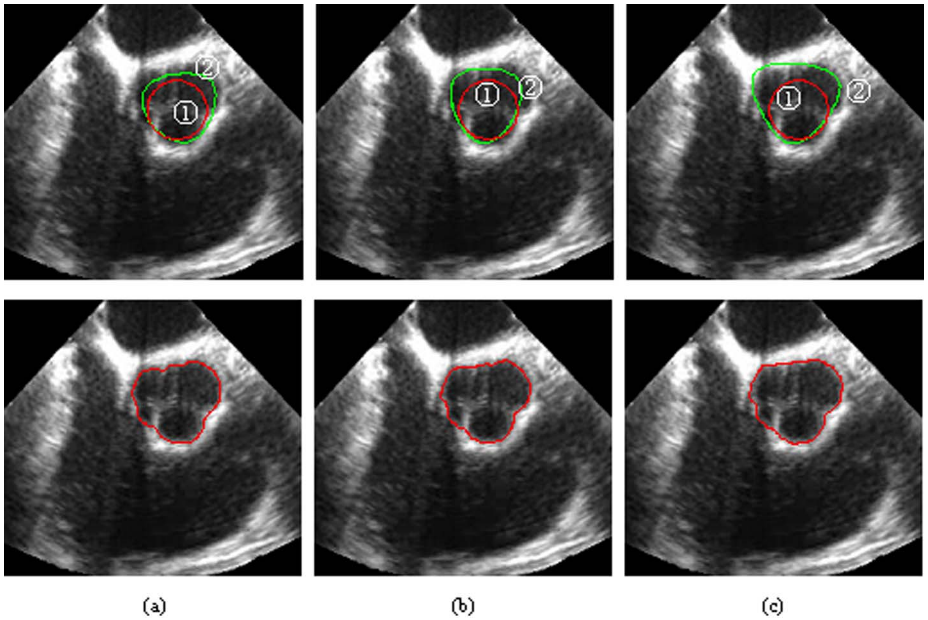

FIG. 8. An example (image size: 224 × 272) shows the influence of the initial constraint shape. In the first row, the closed curves ① show the initial evolution contours and the closed curves ② are the constraint shapes. In the second row, the curves denote the segmentation results.

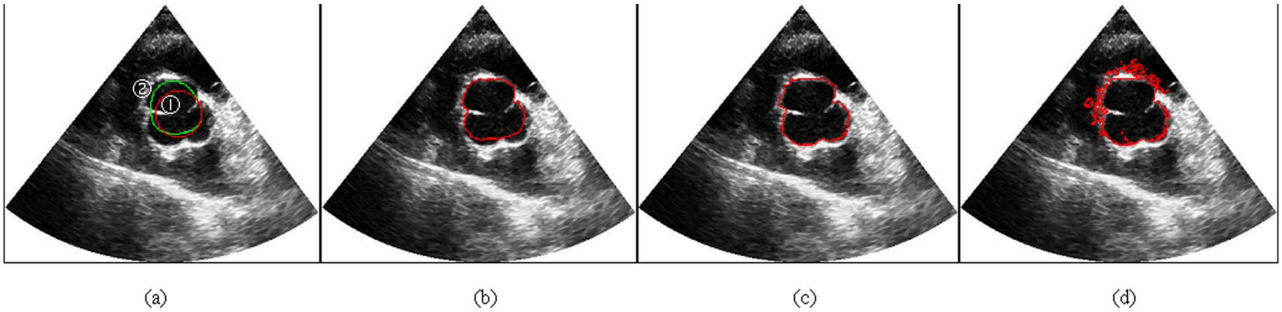

FIG. 9. Analyze the parameter α. In (a) the circle ① denotes the initial evolution curve, and the circle ② denotes the constraint shape. In (b) $\alpha = 0$, $\beta = 0.1$, (c) $\alpha = 0.5$, $\beta = 0.1$, and (d) $\alpha = 1.5$, $\beta = 0.1$, the curve shows the segmentation results.

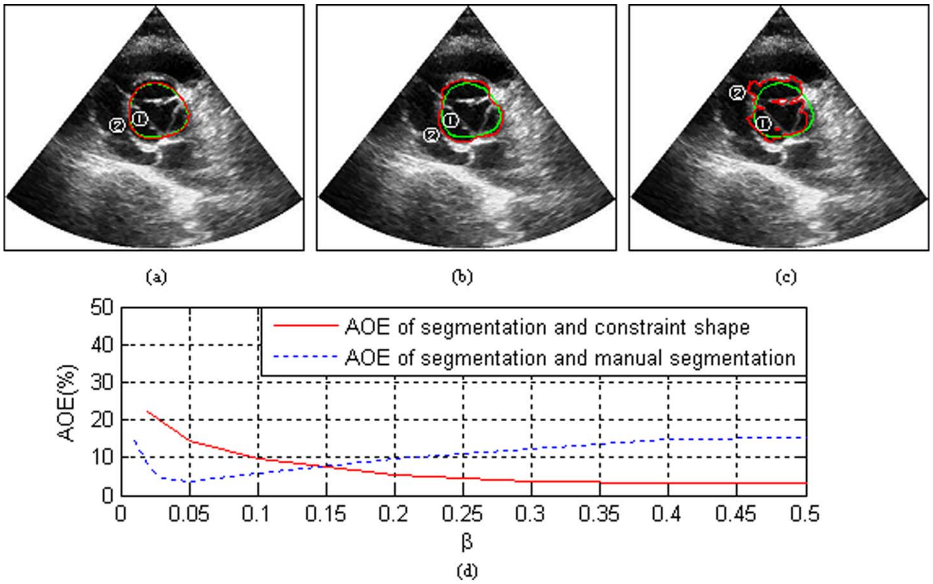

FIG. 10. Analyze the parameter β. In (a), (b), and (c), the curve ② is the evolution contour and the curve ① is the constraint shape, where (a) $\alpha = 0.5$, $\beta = 0.5$; (b) $\alpha = 0.5$, $\beta = 0.05$; (c) $\alpha = 0.5$, $\beta = 0.01$; (d) the solid line is the AOE of the segmentation result and the constraint shape, and the dotted line is the AOE of the segmentation result and the manual segmentation result.

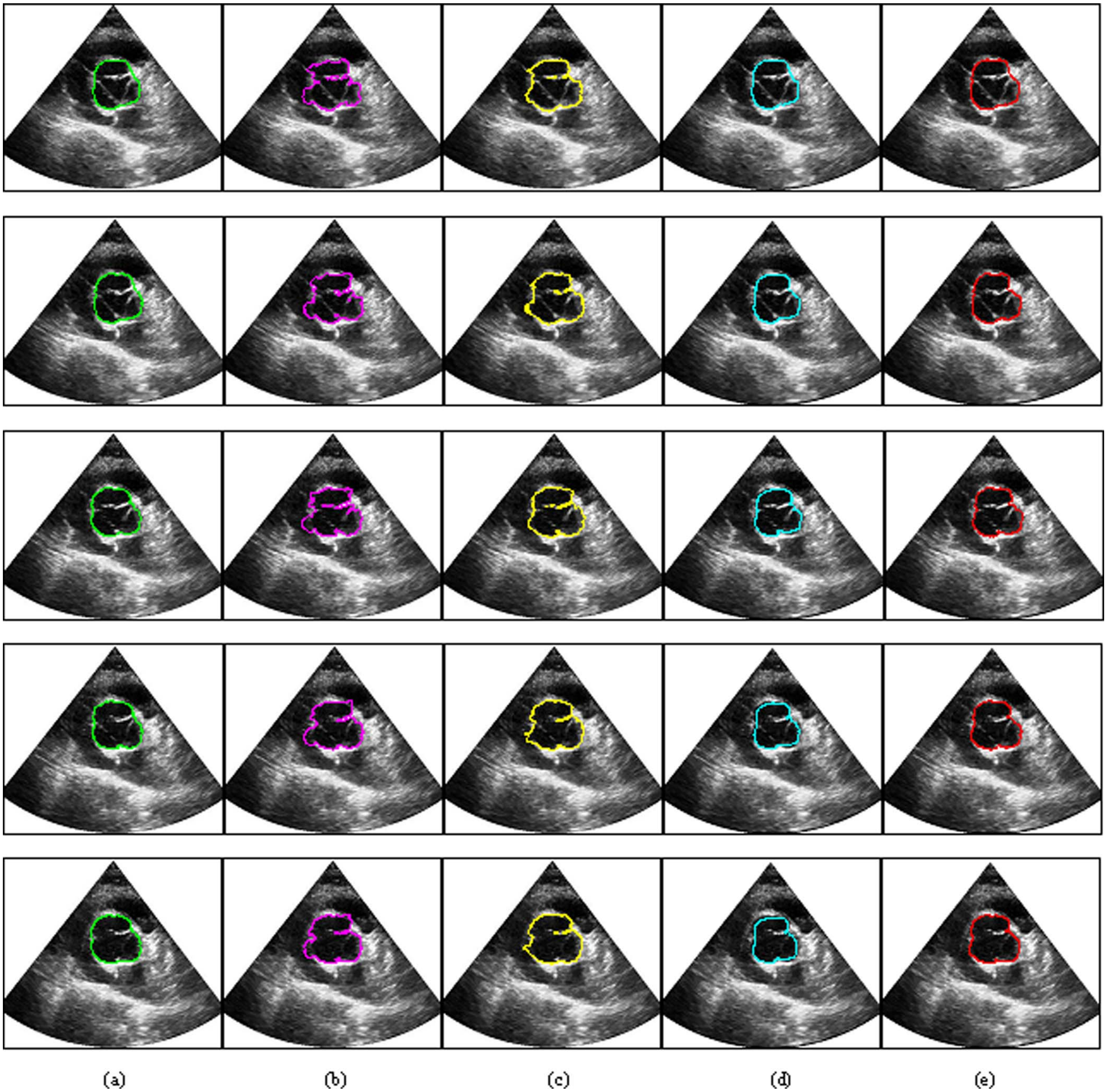

FIG. 11. An example (image size: 636 × 436 pixels; pixel spacing: 0.4336 mm/pixels; iteration step h: 0.01) of the segmentation comparison between the CV model and the proposed method, where five rows represent five continuous sequence AV US images corresponding to sequence images 1–5 (total 35): (a) gold standard; (b) segmentation results by CV model; (c) segmentation results by the GCV model ($\alpha = 0.5$); (d) segmentation results by the shape-constraint CV model ($\beta = 0.05$); (e) segmentation results by the proposed method ($\alpha = 0.5$, $\beta = 0.05$). With the increasing iteration times, both (b) and (c) overflow more and more seriously. Because the results do not converge, the number of iterations is configured as 55 manually.

The segmentation result is obtained by minimizing the proposed energy function.

3. EXPERIMENT

3.A. Experiment data and environment

The experiment focuses on the AV short axis view where the AV B-mode US data are acquired from http://www.echobyweb.com/index.htm, and the Peking Union Medical College Hospital, using a Philips Sonos 5500. They are divided into two categories: one is transthoracic data with transducer frequency 2.5 MHz that is more blurred (five groups each with 35 sequences); the other is transesophageal data with transducer frequency 4.4 MHz with relatively clear boundaries (four groups each with 35 sequences). To obtain the sequence of the AV US images, DirectShow and FFDShow media decoder are used to convert US video into a sequence of images with 224 × 256 pixels or 636 × 436 pixels.

TABLE II. The five evaluation measures of different methods.

Image no	Method	AOE (%)	RAD (%)	ASCD (mm)	RMSD (mm)	MSCD (mm)	Iteration times
1	CV model	19.6056	11.8187	2.6154	4.1532	14.3948	55
	GCV model	16.1777	10.5529	1.6531	2.1617	7.7471	55
	Shape-constraint CV model	8.7339	6.8394	0.5489	0.6895	1.3284	33
	Proposed	4.5547	3.9717	0.4282	0.4933	0.8872	35
2	CV model	18.9830	12.9954	2.4265	3.8826	14.6388	55
	GCV model	15.9651	11.0983	1.7618	2.4705	7.9354	55
	Shape-constraint CV model	9.2311	9.5214	1.3807	1.5744	3.0623	31
	Proposed	9.7029	7.8018	1.2311	1.4758	2.9488	32
3	CV model	15.4084	9.2787	1.9827	3.5177	14.2574	55
	GCV model	10.9925	7.5782	1.2380	2.0980	10.7201	55
	Shape-constraint CV model	11.3818	12.7575	1.3488	1.5493	3.5158	34
	Proposed	8.4213	6.1284	1.1055	1.4526	3.0488	36
4	CV model	12.6575	8.7303	1.3860	2.6924	12.3573	55
	GCV model	10.0833	7.5960	1.0021	1.5620	6.3977	55
	Shape-constraint CV model	12.0899	13.6740	1.5784	1.8803	3.6200	32
	Proposed	7.6315	5.3836	0.6864	0.9439	2.8404	33
5	CV model	11.9166	9.7629	1.0447	2.5895	12.2694	55
	GCV model	10.1575	8.4180	1.7542	1.5396	6.7567	55
	Shape-constraint CV model	13.9524	16.2148	1.6374	2.0972	3.8489	32
	Proposed	7.4623	5.8172	0.7048	0.9813	2.6983	34

The proposed mechanisms are implemented on a desktop PC computer with Pentium® Dual-Core CPU E5800 @ 3.20 GHz, 2 GB RAM, NVIDIA GeForce GT 430 GPU, with Matlab 7.11.0 and VS2008 on Windows XP.

3.B. Experiment processes

Considering the contextual continuity in the US image sequence, the processes of the segmentation scheme are shown in Fig. 5. The complete experimental framework for the implementation of the proposed energy-based segmentation method is summarized by the following steps:

(1) Convert the video into a sequence of images by DirectShow and FFDShow media decoder [Fig. 5(a)];
(2) Extract the fan-shaped ROI [Fig. 5(b)];
(3) Calculate the gradient vector field [Fig. 5(e)], where the GCV model can be constructed by the deviation angle between the inward normal force of the evolution contour and gradient vector flow force;
(4) Define the constraint shape that covers the whole AV region: the initial constraint shape is defined by a cardinal spline though four user-defined points [Fig. 5(c)]; the other constraint shapes are derived from the segmentation result of the adjacent frame [Fig. 5(g)];
(5) Integrate the shape-constraint energy terms into the GCV model by a signed distance map [Fig. 5(d)];
(6) Minimize the shape-constrained GCV model to achieve the AV segmentation results [Fig. 5(f)].

3.C. Evaluation measures

The following five error measures[40] are employed to evaluate the quality of the given segmentations, where smaller error measures represent better segmentation results.

(a) Area-metric overlap error (AOE):

$$m1 = (1 - \frac{R_{\text{seg}} \cap R_{\text{ref}}}{R_{\text{seg}} \cup R_{\text{ref}}}) \times 100\% = \frac{\text{FP}+\text{FN}}{\text{FP}+\text{TP}+\text{FN}} \times 100\%. \tag{10}$$

(b) Relative area difference (RAD):

$$m_2 = \frac{|R_{\text{seg}} - R_{\text{ref}}|}{R_{\text{ref}}} \times 100\%. \tag{11}$$

(c) Average symmetric contour distance (ASCD):

$$m_3 = \frac{\sum_{a\in A}[\min_{b\in B}\{\text{dist}(a,b)\}] + \sum_{b\in B}[\min_{a\in A}\{\text{dist}(a,b)\}]}{N_A + N_B}. \tag{12}$$

(d) Root mean square symmetric contour distance (RMSD):

$$m_4 = \sqrt{\frac{\sum_{a\in A}[\min_{b\in B}\{\text{dist}(a,b)\}]^2 + \sum_{b\in B}[\min_{a\in A}\{\text{dist}(a,b)\}]^2}{N_A + N_B}}. \tag{13}$$

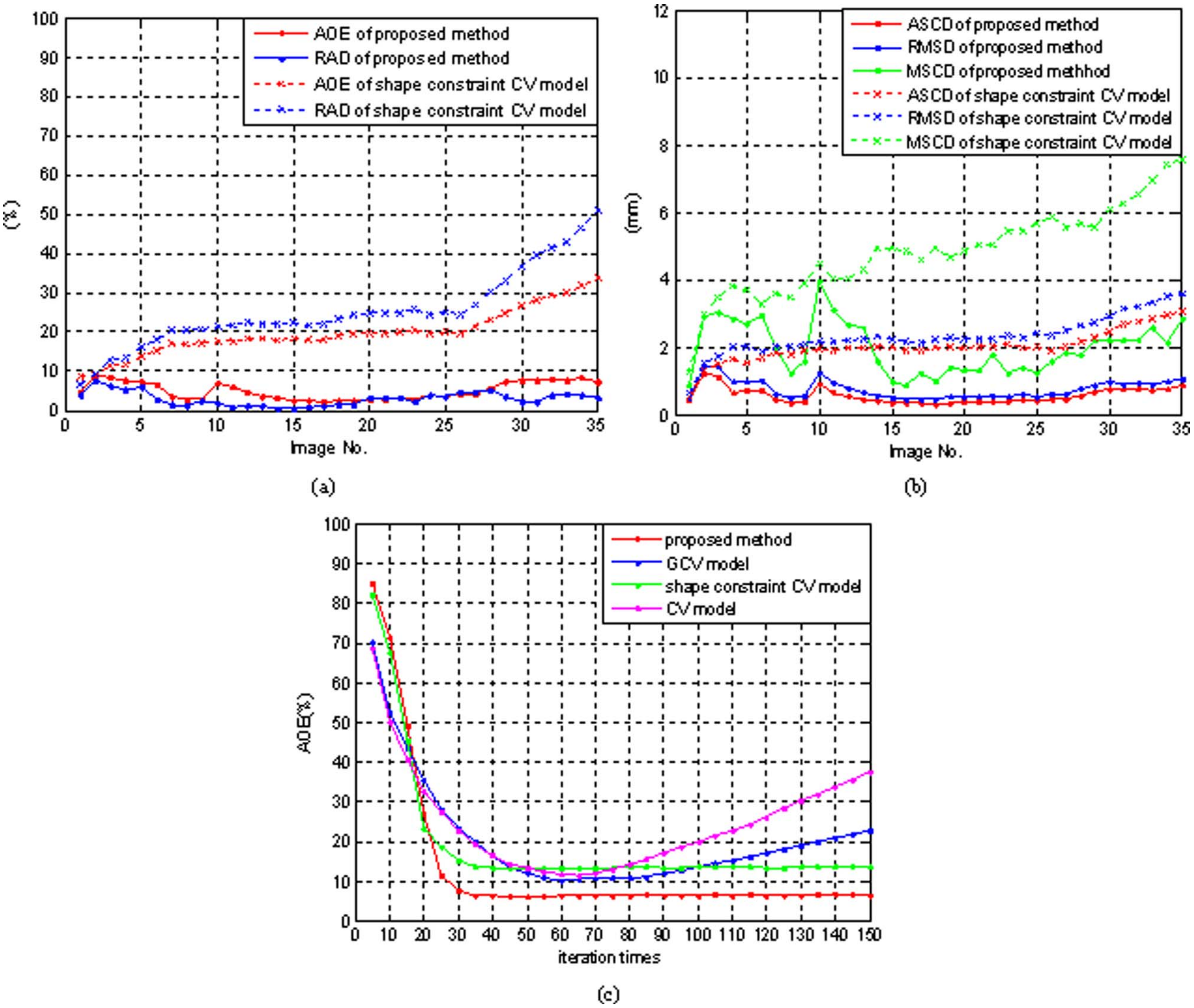

(a)

(b)

(c)

FIG. 12. (a) and (b) show the comparison of the segmentation results using the shape-constraint CV model and the proposed method with the increasing image numbers (total 35, Image No. 1–5 corresponding five rows in Fig. 11); (c) describes one AV US image (Image No. 5) using the proposed method compared with the other methods with the increasing iteration times (iteration step h is 0.01).

(e) Maximum symmetric contour distance (MSCD):

$$m_5 = \max\left\{\max_{a\in A}\left\{\min_{b\in B}\{\mathrm{dist}(a,b)\}\right\},\right.$$
$$\left.\times\max_{b\in B}\left\{\min_{a\in A}\left\{\mathrm{dist}(a,b)\right\}\right\}\right\}. \quad (14)$$

Among the above five evaluation measures, R_{seg} and R_{ref} denote the pixel set of the region by the proposed method and radiologist, respectively (as shown in Fig. 6, $R_{\mathrm{seg}} = \mathrm{FP} + \mathrm{TP}$, $R_{\mathrm{ref}} = \mathrm{TP} + \mathrm{FN}$), A and B denote the edges of R_{seg} and R_{ref}, respectively, dist(a, b) denotes the distance between pixel a and pixel b, and N_A and N_B denote the total numbers of pixels on A and B, respectively.

3.D. The initialization and initial constraint shape

A change in the position, size, or shape of the initial contour has little influence on the final segmentation result, since the shape-constraint energy drive the evolution contour to the AV region. Figure 7 shows that although the position, size, and shape of the initial contours are different (note that the constraint shapes are the same as indicated by the closed curves ②), the segmentation results are similar. Under the circumstances, a circle can be specified as the initial evolution contour in our experiments.

The repeatability of the proposed method is shown in Fig. 8, in which the AV is segmented using this method with different initial manually defined constraint shapes, and where the segmentation results are almost the same. The AV can be segmented accurately as long as the manually defined shape roughly covers the AV region.

3.E. Parameter estimation

It is important to select proper parameters of the model for better image segmentation. The empirical values of two

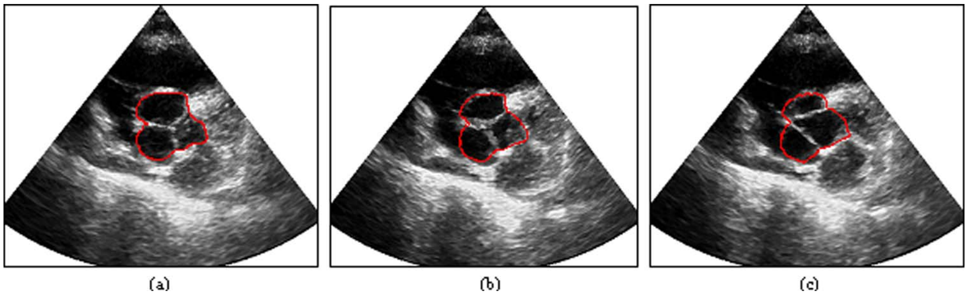
(a) (b) (c)

FIG. 13. The segmentation results of the proposed method: (a) No. 31, (b) No. 32, and (c) No. 33.

parameters are determined by a sufficient number of repeatable experiments.

One of these is the weight of the gradient vector force α. If it is too big, the extending capture range of the force field will add noise, as shown in Fig. 9(d); if it is too small, the shape-constraint energy has a predominant function on the evolution contour where the segmentation result may be similar to the constraint shape [Fig. 9(b)]. As shown in Fig. 9(c), the appropriate α drives the evolution contour to the ideal boundary, where the proper range of variation α is chosen from 0.3 to 1 in our experiment.

Another parameter is the weight of the shape-constraint β. If it is too large, the segmentation result may simply become the predefined constraint shape [Fig. 10(a)]. Otherwise, the segmentation result may overflow at the weak edges or miss part of the AV [Fig. 10(c)] because the shape-driven energy has less influence on the surface evolution. As shown in Figs. 10(b) and 10(d), the successful segmentation results are

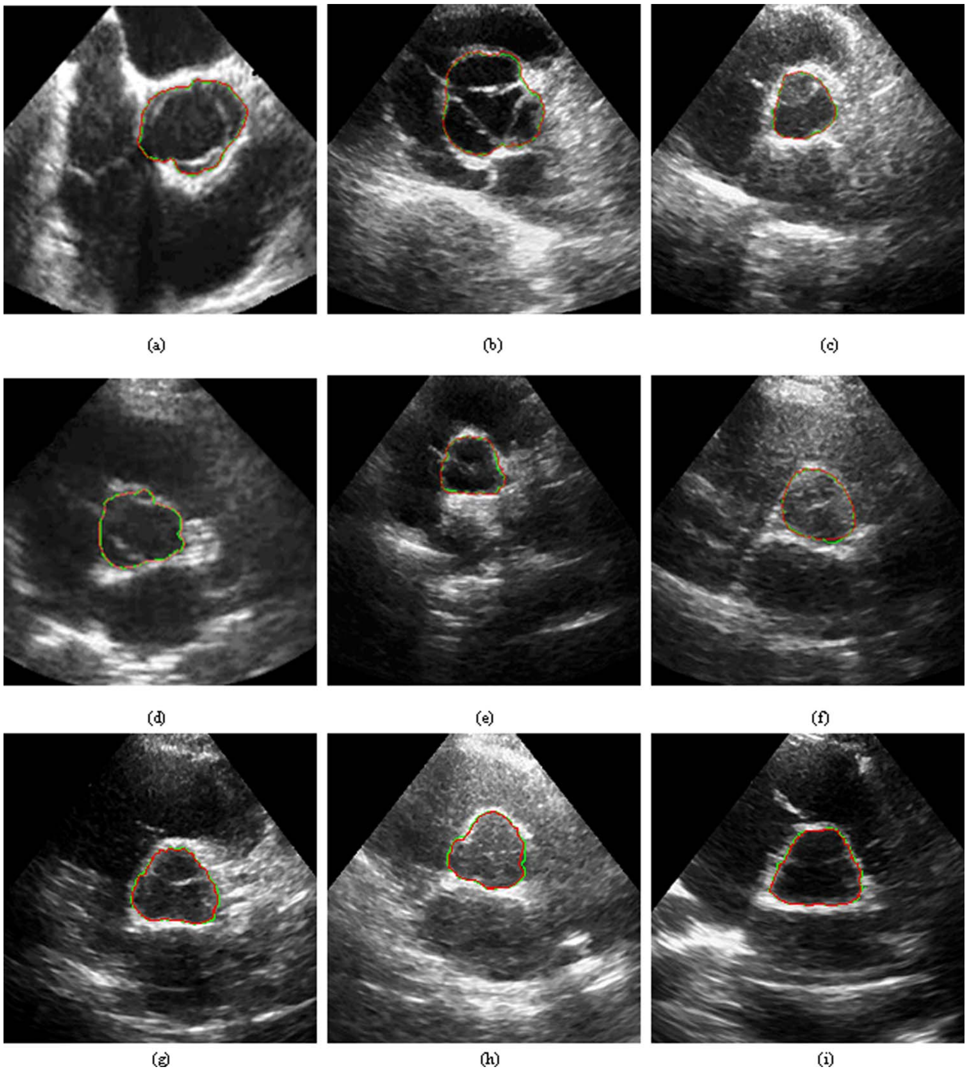
(a) (b) (c) (d) (e) (f) (g) (h) (i)

FIG. 14. The AV segmentation comparisons between our method and the gold standard method, where nine groups correspond to (a)–(i).

TABLE III. AV segmentation results for each measure are reported as mean and standard deviation over all test images.

No.	Image size	Pixel spacing (mm/pixel)	AOE (%)	RAD (%)	ASCD (mm)	RMSD (mm)	MSCD (mm)
(a)	224 × 272	0.4646	5.5970 ± 1.1541	2.4850 ± 1.3202	0.7490 ± 0.1522	0.9690 ± 0.1844	2.3759 ± 0.7361
(b)	636 × 436	0.4336	4.9886 ± 2.0702	2.0331 ± 1.7060	0.6951 ± 0.1625	0.8813 ± 0.1541	1.6853 ± 0.4403
(c)	636 × 436	0.4737	6.0166 ± 1.8814	3.8726 ± 2.8759	1.1504 ± 0.4800	1.6134 ± 0.6330	3.3730 ± 0.8308
(d)	224 × 256	0.5059	9.1806 ± 2.4367	4.5168 ± 1.9936	1.3870 ± 0.3966	1.9206 ± 0.5460	4.9157 ± 1.5578
(e)	636 × 436	0.5326	5.7238 ± 1.3389	3.4328 ± 2.1863	0.7797 ± 0.1262	1.3630 ± 0.4535	3.4812 ± 0.7921
(f)	636 × 436	0.5020	9.5354 ± 3.4956	6.1406 ± 3.2860	1.5762 ± 0.3742	1.7451 ± 0.4643	5.2400 ± 2.2363
(g)	636 × 436	0.4737	5.3684 ± 0.9064	3.5914 ± 1.2591	0.9799 ± 0.3977	0.9639 ± 0.1154	2.1484 ± 0.4006
(h)	636 × 436	0.5326	8.4147 ± 3.7185	4.5850 ± 2.8574	1.1823 ± 0.3552	1.4748 ± 0.2543	4.5857 ± 1.1663
(i)	636 × 436	0.4737	7.2170 ± 2.8168	4.7819 ± 2.9881	1.2117 ± 0.2147	1.4419 ± 0.3810	4.3110 ± 1.4708
Total			6.8936 ± 2.8839	3.9377 ± 2.6316	1.0790 ± 0.4260	1.3748 ± 0.5220	3.5685 ± 1.7159

acquired by setting the appropriate parameter, where the optimum range of β is between 0.02 and 0.2.

3.F. The comparison of segmentation results among different methods

Below we provide a detailed comparison of the shape-constrained GCV model with other methods.

As the position and shape of AV are changed slightly in adjacent images that have a strong time correlation, the segmentation result of the adjacent image is used to reduce the user interactions and improve the efficiency. Here, the constraint shape of the first image is constructed by the cardinal spline that passes through four user-defined points, and the other four constraint shapes are constructed from the previous image. The segmentation result can be calculated by minimizing the GCV model with shape-constrained energy.

As shown in Fig. 11, the serious overflow occurs at weak boundaries when the CV model is employed [Fig. 11(b)]. Although the overflow is suppressed by the GCV model [Fig. 11(c)] the overflow still occurs. In Fig. 11(d), the shape constraint prevents any overflow in the CV model, but the under segmentation error accumulates with the increasing number of processed sequence images. The gradient vector energy enlarges the capture range of the external force, allowing the evolution contour to better access the details instead of losing them by using shape-constraint CV model. The segmentation results of the proposed method [Fig. 11(e)] achieved the best correlation to the gold standard [Fig. 11(a)]; Consequently, the dual role of both the gradient vector and shape-constrained energies that enhance the image weak edge force, cause the evolution contour to approach that of the target more accurately. Five error measures are employed to evaluate the accuracy of the segmentation results as shown in Table II.

Figure 12 explains why both the shape constraint and the gradient vector energy need to be added to the CV model.

With the increasing iteration times (iteration times > 60) [Fig. 12(c)], the AOE of the CV model increases rapidly, because it seriously overflows at weak boundaries. The AOE of the GCV model increases slowly where the overflow rate is slowing down, where the AOE of the shape-constraint CV model and the proposed method tend to be steady, although the AOE of the shape-constraint CV model is bigger than the proposed method. Since the shape-constraint energy acts on the evolution contour, there is no overflow and the number of iterations is significantly reduced.

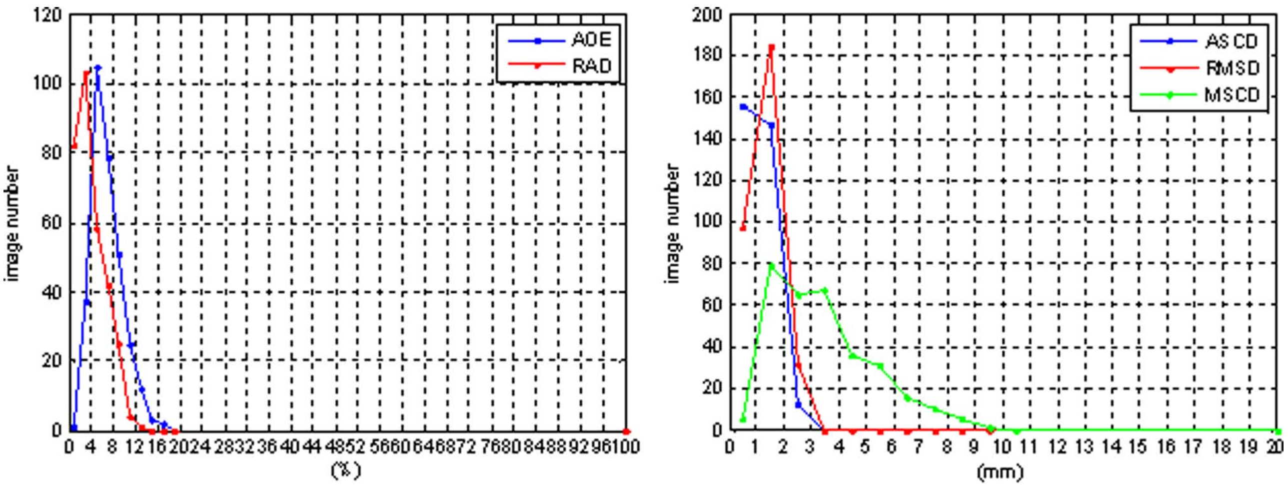

(a) (b)

FIG. 15. The distribution map of evaluation parameters between the proposed segmentation results and the gold standards. Each point (total 315) shows the number of images with the specified range. (a) represents the distribution map of AOE and RAD; (b) shows the distribution map of ASCD, RMSD, and MSCD.

Then we describe these two convergent methods, i.e., the shape-constraint CV model and the proposed method in more detail. As shown in Figs. 12(a) and 12(b), segmentations using these two methods (on a group with 35 image sequence) are evaluated by five measures. With the increasing image numbers, there are growing values of error measures by using the shape-constraint CV model, but stable ranges by using the proposed method. The gradient vector energy eliminates the accumulation of errors, where it allows the evolution contour better access to the details and overcome the problem of loss of detail using the shape-constraint CV model.

Among the 35 image sequences from No. 31 to No. 33, the largest change in AV shapes occurred during one beating circle when the AV is opening (Fig. 13), where the proposed approach can eventually resolve the situation properly.

3.G. Assessment of segmentation results

As shown in Fig. 14, nine groups of data, each with 35 image sequences were segmented using the proposed method and by an expert. Five errors were measured to evaluate our segmented results, where the accuracy varied on the quality of the data. Table III (a)–(i) represents the evaluation measures of the nine groups in Figs. 14(a)–14(i), respectively.

With the increasing abscissa values, the number of images tends to zero [Figs. 15(a) and 15(b)]. These experiments demonstrate that the proposed method is feasible to help physicians during image-guided cardiac interventions.

4. CONCLUSIONS

In this paper, a novel energy-based active contour approach, the shape-constraint GCV model, has been proposed for segmenting the AV from sequenced US images. A major contribution of this paper is that it provides an accurate and robust AV US image segmentation method which is the adaptation of the CV model combining with both gradient vector energy and a shape-driven energy. The gradient vector energy is added into the CV model to form the GCV model framework by calculating the deviation angle between the inward normal force of the evolution contour and the gradient vector flow force. The gradient vector energy enhances the weak boundary as the gradient vector external force field extends the capture range to the whole image domain by diffusing the forces. The shape-constraint energy is integrated to the GCV model by a shape comparison function to force the active contour into an ideal contour. In this way, the AV can be segmented from US images accurately and robustly. The other contribution of this paper is that the proposed method improves efficiency and reduces the workload of physicians. The radiologist only needs to define four points in the AV region to acquire a sequence of AV segmentation results, where the initial constraint shape is constructed by four manually defined points, and other constraint shapes can be obtained from calculating the segmented results of the adjacent US frame by morphology filtering.

Compared with the traditional CV model, the proposed shape-constrained GCV method can segment the AV more efficiently and accurately. For validation, we compared the performance of our approach against the gold standard, using data from nine patients, each having 35 AV US images, and demonstrated that out method can segment the AV effectively. We believe the shape-constraint GCV approach can play an important role in image guided TAVI intervention[41] and computer-aided diagnoses of cardiac disease.

Our future work will generally concern on two directions: one is how to pursue real-time performance using substantial clinical data, another is how to accurately and effectively track the AV contour from the poorer US images.

ACKNOWLEDGMENTS

This research work is partially supported by the Chinese NSFC research Fund (61190120-61190124 and 61271318). The authors are grateful to the clinicians of the Peking Union Medical College Hospital for their support in providing image data and clinical advice.

[a] Authors to whom correspondence should be addressed. Electronic addresses: xiehongzhi@medmail.com.cn and gulixu@sjtu.edu.cn; Telephone: +86 (021)62933250; Fax: +86 (021)62933250.

[1] J. T. Butcher, C. A. Simmons, and J. N. Warnock, "Review: Mechanobiology of the aortic heart valve," J. Heart Valve Dis. **17**(1), 62–73 (2008).

[2] S. H. Rahimtoola, "The year in valvular heart disease," J. Am. Coll. Cardiol. **60**(2), 85–95 (2012).

[3] E. J. Howell and J. T. Butcher, "Valvular heart diseases in the developing world: Developmental biology takes center stage," J. Heart Valve Dis. **21**(2), 234–240 (2012).

[4] Z. Luo *et al.*, "A pilot study on magnetic navigation for transcatheter aortic valve implantation using dynamic aortic model and US image guidance," Intl. J. Comput. Assist. Radiol. Surg. **8**(4), 677–690 (2013).

[5] W. W. Parmley and L. Talbot, "Heart as a pump," *Handbook of Physiology: Sec. 2: The Cardiovascular System, Vol. 1: The Heart* (Oxford University Press, New York, 1979), Vol. 1, pp. 429–460.

[6] R. G. Dantas and E. T. Costa, "Ultrasound speckle and equivalent scatterers," Ultrasonics **43**(6), 405–420 (2005).

[7] J. Alison Noble and D. Boukerroui, "Ultrasound image segmentation: A survey," IEEE Trans. Med. Imaging **25**(8), 987–1010 (2006).

[8] N. Yuanyuan *et al.*, "A novel aortic valve segmentation from ultrasound image using continuous max-flow approach, in *Proceedings of the 35th Annual International Conference on Engineering in Medicine and Biology Society (EMBC)* (IEEE, Piscataway, NJ, 2013), pp. 3311–3314.

[9] S. Sridevi, and M. Sundaresan, "Survey of image segmentation algorithms on ultrasound medical images," in *Proceedings of the International Conference on Pattern Recognition, Informatics and Medical Engineering (PRIME)* (IEEE, Piscataway, NJ, 2013), pp. 215–220.

[10] K. Saini, M. L. Dewal, and M. K. Rohit, "Ultrasound imaging and image segmentation in the area of ultrasound: A review," Intl. J. Adv. Sci. Technol. **24**, 41–60 (2010).

[11] W. J. Sarmiento, A. Lozano, and E. Romero, "Cardiac tissue segmentation in ultrasound images using histogram of absolute differences," in *Proceedings of the IEEE International Workshop on Biomedical Circuits and Systems* (IEEE, Piscataway, NJ, 2004), pp. S3/4–S1-4.

[12] Y. Zimmerand, R. Tepper and S. Akselrod, "A two-dimensional extension of minimum cross entropy thresholding for the segmentation of US images," Ultrasound Med. Biol. **22**, 1183–1190 (1996).

[13] J. Klingler *et al.*, "Segmentation of echocardiographic images using mathematical morphology," IEEE Trans. Biomed. Eng. **35**, 925–934 (1988).

[14] N. Shanmugam *et al.*, "A novel approach to medical image segmentation," J. Comput. Sci. **7**(5), 657–663 (2011).

[15] M. Ruben *et al.*, "Segmentation of ventricular angiographic images using fuzzy clustering," in *Proceedings of the IEEE 17th Annual Conference*

on Engineering in Medicine and Biology Society (IEEE, Piscataway, NJ, 1995), Vol. 1, pp. 405–406.

[16] J. Shan, H. D. Cheng, and Y. Wang, "A novel segmentation method for breast ultrasound images based on neutrosophic l-means clustering," Med. Phys. **39**, 5669–5682 (2012).

[17] S. Nandagopalan *et al.*, "Automatic segmentation and ventricular border detection of 2D echocardiographic images combining K-means clustering and active contour model," in *Proceedings of the Second International Conference on Computer and Network Technology (ICCNT)* (IEEE, Piscataway, NJ, 2010), pp. 447–451.

[18] P. Bansod, U. B. Desai, and N. Burkule, "Endocardial segmentation in contrast echocardiography video with density based spatio-temporal clustering," in *Proceedings of the First International Conference on Bio-inspired Systems and Signal Processing* (Springer, Berlin, 2008), 204–209.

[19] Li Qianqian *et al.*, "An improved method based on CV and snake model for ultrasound image segmentation," in *Proceedings of the Seventh International Conference on Image and Graphics (ICIG)* (IEEE, Piscataway, NJ, 2013), pp. 160–163.

[20] X. Qian *et al.*, "Segmentation of rat cardiac ultrasound images with large dropout regions," in *Proceedings of the Conference on Computer Vision and Pattern Recognition Workshop, 2006, CVPRW'06* (IEEE, Piscataway, NJ, 2006), pp. 93–93.

[21] S. Osher and J. A. Sethian, "Fronts propagating with curvature-dependent speed: Algorithms based on Hamilton-Jacobi formulations," J. Comput. Phys. **79**(1), 12–49 (1988).

[22] V. Caselles, R. Kimmel, and G. Sapiro, "Geodesic active contours," Intl. J. Comput. Vis. **22**(1), 61–79 (1997).

[23] C. Li *et al.*, "Level set evolution without re-initialization: A new variational formulation," in *Proceedings of the IEEE Computer Society Conference on Computer Vision and Pattern Recognition, 2005, CVPR 2005* (IEEE, Piscataway, NJ, 2005), Vol. 1, pp. 430-436.

[24] D. Mumford and J. Shah, "Optimal approximation by piecewise smooth functions and associated variational problems," Commun. Pure Appl. Math. **42**, 577–685 (1989).

[25] T. Chan and L. Vese, "Active contours without edges," IEEE Trans. Image Process. **10**(2), 266–277 (2001).

[26] L. A. Vese and T. F. Chan, "A multiphase level set framework for image segmentation using the Mumford and Shah model," Intl. J. Comput. Vis. **50**(3), 271–293 (2002).

[27] A. Belaid *et al.*, "Phase-based level set segmentation of ultrasound images," IEEE Trans. Inf. Technol. Biomed. **15**(1), 138–147 (2011).

[28] Y. Shang *et al.*, "Prior based cardiac valve segmentation in echocardiographic sequences: Geodesic active contour guided by region and shape prior," *Pattern Recognition and Image Analysis* (Springer, Berlin, 2005), pp. 447–454.

[29] S. Martin *et al.*, "Fast segmentation of the mitral valve leaflet in echocardiography," *Computer Vision Approaches to Medical Image Analysis* (Springer, Berlin, 2006), pp. 225–235.

[30] C. Xu and J. L. Prince, "Snakes, shapes, and gradient vector flow," IEEE Trans. Image Proces. **7**(3), 359–369 (1998).

[31] C. Xu and J. L. Prince, "Gradient vector flow: A new external force for snakes," in *Proceedings of the IEEE Computer Society Conference on Computer Vision and Pattern Recognition* (IEEE, Piscataway, NJ, 1997), pp. 66–71.

[32] D. Cremers, N. Sochen, and C. Schnorr, "Towards recognition-based variational segmentation using shape priors and dynamic labeling," in *International Conference on Scale Space Theories in Computer Vsion*, Lecture Notes in Computer Science Vol. 2695, edited by L. Griffith (Springer Berlin Heidelberg, 2003), pp. 388–400.

[33] B. Dong *et al.*, "Aortic valve segmentation from ultrasound images based on shape constraint CV model," in *Proceedings of the 35th Annual International IEEE Conference on Engineering in Medicine and Biology Society (EMBC)* (IEEE, Piscataway, NJ, 2013), pp. 1402–1405.

[34] C. Li *et al.*, "Level set evolution without re-initialization: A new variational formulation," in *Proceedings of the IEEE Computer Society Conference on Computer Vision and Pattern Recognition, 2005, CVPR 2005* (IEEE, Piscataway, NJ, 2005), Vol. 1, pp. 430–436.

[35] C. Li *et al.*, "A level set method for image segmentation in the presence of intensity inhomogeneities with application to MRI," IEEE Trans. Image Proces. **20**(7), 2007–2016 (2011).

[36] S. Osher and R. Fedkiw, *Level Set Methods and Dynamic Implicit Surfaces [M]* (Springer, Berlin, 2003), Vol. 153.

[37] R. Courant and D. Hilbert, *Methods of Mathematical Physics* (Interscience, New York, 1953), Vol. 1.

[38] I. J. Schoenberg and I. J. Schoenberg, *Cardinal Spline Interpolation. [M]* (Society for Industrial and Applied Mathematics, Philadelphia, 1973), Vol. 12.

[39] J. Serra, *Image Analysis and Mathematical Morphology* (Academic Press, New York, 1982).

[40] B. Sahiner *et al.*, "Computer-aided characterization of mammographic masses: Accuracy of mass segmentation and its effects on characterization," IEEE Trans. Med. Imaging **20**(12), 1275–1284 (2001).

[41] Z. Luo, J. Cai, T. M. Peters, and L. Gu, "Intra-operative 2-D ultrasound and dynamic 3-D aortic model registration for magnetic navigation of transcatheter aortic valve implantation," IEEE Trans. Med. Imaging **32**(11), 2152–2165 (2013).